SLAC-PUB-6241
SLAC/SSRL-0034
May 1993
(SSRL-M)

IMAGING BAND PASS ANALYZER (BPA) USING DOUBLE 90 DEGREE SPHERICAL ANALYZERS*

Changyoung Kim, Paul L. King, Piero Pianetta
Stanford Linear Accelerator Center, Stanford Synchrotron Radiation Laboratory
Stanford, CA 94309, U.S.A.

Michael A. Kelly
Material Science Engineering, Stanford University
Stanford, CA 94305, U.S.A.

Charles A. Bryson
Surface/Interface
Mountain View, CA 94041, U.S.A.

Abstract

The design and testing of an imaging band pass analyzer (BPA) consisting of two 90° spherical sectors operating in a magnetic field free region is described. Image electrons injected nearly parallel to one another and perpendicular to the first 90° sector are focused into an energy plane where electrons of desired energy are band-pass filtered. A second 90° sector is used to recover the energy-filtered image. With a 1 mm aperture, energy resolution of 1% and spatial resolution of 0.01% of the main path radius are calculated and agree well with the test results over an image size of 12x12 mm^2. The addition of this analyzer to our magnetic projection photoelectron microscope poses an additional technological problem in that the electrons are required to pass from a relatively high field area to a field free region without disruption of the image. Design considerations for a structure that abruptly terminates a magnetic field yet is transparent to image electrons are described.

Paper submitted to Review of Scientific Instruments

* Work Supported by the U.S. Department of Energy under Contract DE-AC03-76F00515

1. Introduction

X-ray photoelectron spectroscopy(XPS) took on its modern form with emphasis on core level analysis in the mid-1950s[1]. Since that time the technique has progressed by both incremental and radical improvements in vacuum hardware, spectrometer construction and x-ray source design leading to the high level of performance found in today's commercial systems. Innovations have been pursued precisely because the strengths of the technique - its surface sensitivity, access to chemical state information, relative ease of quantification, and non-destructive character - are firmly established and offer recognized problem solving capabilities to surface scientists in both research and production environments.

A frequently cited drawback of XPS and a specific concern that continues to motivate developmental efforts is that the relatively poor lateral resolution of XPS compared to other surface techniques such as electron stimulated Auger analysis(AES) or secondary ion mass spectrometry(SIMS). The root cause of this discrepancy is that it is far easier to produce and focus intense beams of charged particles than to produce and focus intense beams of x-rays. Conventional XPS systems probe areas on the order of square millimeters where, by comparison, sub-micron Auger analysis can be considered commonplace.

Strategies for improving lateral resolution in XPS can be separated into those techniques in which x-rays are focused to a fine point and those that make use of the imaging properties of transfer lens optics and electron analyzer optics. *Focusing* techniques (x-ray microprobes) have been pursued commercially by Surface Science Instruments[2] as well as in research environments at a number of synchrotron facilities[3][4][5]. *Imaging* systems that bring practical measurements below the 100 μm range have recently been described in the literature[6][7][8]. These imaging strategies can be further distinguished by the manner in which they transfer and magnify the image of the emitting source and by the method of energy filtering. Given the advantage of parallel analysis over serial analysis, the combination of transfer optics and spectrometer which are both compatible with imaging represents a desirable goal.

This paper describes the design and testing of an electron spectrometer that is compatible with imaging. This band-pass spectrometer has been designed to complement a magnetic projection photoelectron microscope which acts as the front-end transfer and magnifying optics for an advanced photoelectron imaging system[9]. The magnifying properties of magnetic projection microscopy were first developed in the Turner group at Oxford[10] and are unique in that the sample sits in a large magnetic field produced by a solenoid(Fig. 1). Collection efficiency approaches 100% with photoelectrons following helical paths tangential to guiding magnetic field lines. The image is magnified as the field lines diverges with the magnification dependent on the ratio of the fields at the sample and at the image plane. Magnetic projection in a diverging field also has useful parallelizing effects by which the helical paths followed by the electrons unwind as the field diverges[11]. Assuming a 200 μm field of view and magnification of 70x, magnetic projection offers the spectrometer a relatively large magnified image of source emission(~10 mm in diameter) in which the electrons are moving nearly parallel to one another. To date our microscope has been operated with a simple retarding analyzer[12] and the development of an imaging band pass analyzer is being pursued in order to improve signal to noise levels in x-ray excited, energy filtered imaging.

There are two key challenges taken up in this work. First, in entering the double-hemispherical analyzer, the magnified image must pass from an area containing a magnetic field(~15 Gauss) into a field free region with minimal disruption to the image. Section 2 describes the design and optical properties of a magnetic terminating assembly that is largely transparent to electrons. Second, the relatively large, low angular dispersion image found in the field free region must be filtered with good energy resolution and with minimal disruption to the image. Section 3 describes an imaging band pass analyzer in which two 90° spherical sectors are combined. As imaging electrons are injected into the analyzer moving nearly parallel to one another, they form energy dispersed distribution after passing through the first 90° sector. Apertures present between the sectors band-pass filter the electrons with the second 90° sector acting to reform the image. Energy resolution is shown to be limited by the angular dispersion of the electrons originating in

the magnetic projection process and passage through the magnetic terminating assembly and by the size of the images. Section 4 is devoted to a discussion of fringe field effects associated with passage through the analyzer while Section 5 reports recent test results.

2. Calculation of the mesh size for magnetic shielding.

Since the analyzer should be operated in a magnetic field free region, the field from the superconducting magnet needs to be terminated. A magnetic field termination mesh can be used for this purpose. In entering the double-hemispherical analyzer through this mesh, the magnified image must pass from a magnetic field region to a field free region with minimal disruption. As will be shown in section 3, most of the aberrations in energy and spatial resolution come from the angular dispersion of the imaging electrons. The angular dispersion comes from three sources. First, the angular dispersion may come from the divergence of the magnetic field itself. Assuming that the superconducting magnet is a dipole, the magnetic field in front of the analyzer which is 1.5 m away from the magnet has a maximum angle of 0.005 rad, which practically can be neglected. But it can be reduced by using a plate of magnetic material placed in front of the analyzer perpendicular to the magnetic field, which makes the field lines parallel to each other and perpendicular to the plate. Second, the angular dispersion can also come from the fact that electrons are emitted from the sample with a large solid angle. Even though electrons become parallel to the magnetic field as they reach the low field region, the angle is not yet zero when they reach the magnetic mesh. The angle is given by the formula[10]:

$$\sin(\beta_i) / \sin(\beta_f) = (B_i / B_f)^{1/2} \qquad (1)$$

where β_i is the initial angle at the sample surface, β_f the final angle at the detector and B_i, B_f initial and final magnetic field. So for $\beta_i = 45^o$, $\beta_f = 0.7^o = 0.01$ rad. Third, the angular dispersion can come from the deflection of the electrons by the magnetic field as it is terminated by the magnetic

mesh. The magnetic mesh introduces transverse magnetic fields which deflect the electrons thereby introducing an additional angular dispersion. It is desirable to keep the angular dispersion due to this latter effect comparable to or less than that introduced by the first two effects described above which is approximately 0.01 rad.

In order to keep the angular dispersion of the electrons within the 0.01 rad limit, it is important to consider the effect of the mesh which terminates the magnetic field. Since the deflection(or transverse magnetic field) increases as the mesh size increases, reducing the mesh size would remove this problem. But this in turn would also reduce the transparency of the mesh. So the optimum size of the magnetic mesh needs to be decided by considering both the angular dispersion of the transmitted electrons and transparency of the mesh. To calculate the deflection of the electrons going through the mesh by the transverse magnetic fields, we consider a plane with *infinite* permeability(this is a good approximation since some materials have a permeability of more than 10,000) with a hole of arbitrary shape(Fig. 2). The magnetic field on one side of the plane is B_0 and that on the other side zero. Away from the hole, the magnetic field is perpendicular to the plane. But around the hole, the magnetic field has transverse components, which might increase the transverse momenta of the electrons. This results in increased angular dispersion. Let B_t be the transverse component of the magnetic field around the hole. An electron with momentum p would have Lorentz force

$$F = eB_t p / m \tag{2}$$

where e and m are the electron charge and mass. Therefore the total momentum change while this electron goes through the hole is:

$$\Delta p = \left|\int_{-\infty}^{\infty} \vec{F} dt\right| \approx \left|\frac{1}{v_0}\int_{-\infty}^{\infty} \vec{F} dz\right| = \frac{e}{c}\int_{-\infty}^{\infty} B_t \, dz \tag{3}$$

where v_0=p/m is the initial velocity of the electron, e and c are the electron charge and the speed of light, respectively. Δp is assumed to be relatively small compared to p. z is the direction of the magnetic field. B_t needs to be integrated along the electron path. The magnetic potential can be expanded in cylindrical co-ordinates[13]:

$$\Phi^{tot} = \Phi^0 + \Phi^1 \tag{4}$$

and

$$\Phi^1 = \int_{-\infty}^{\infty} \int_{-\infty}^{\infty} A(k_x, k_y) \exp(i(k_x x + k_y y)) \exp(-k|z|) dk_x dk_y \tag{5}$$

where $k^2 = k^2_x + k^2_y$ and $A(k_x,k_y)$ is the expansion coefficient. Φ^{tot} is the total magnetic potential and Φ^0 is the potential of the uniform magnetic field and Φ^1 is the perturbed potential due to the hole. This perturbed potential satisfies boundary conditions[13]:

$$\left[\partial\Phi^1 / \partial Z\right]_{Z=0} = -\frac{1}{2} B_0 \qquad \text{when (x,y) is in the hole} \tag{6}$$

$$\left[\partial\Phi^1 / \partial Z\right]_{Z=0} = 0 \qquad \text{when (x,y) is not in the hole} \tag{7}$$

Then the change of the momentum due to the terminated magnetic field becomes:

$$\Delta\vec{p} \approx \frac{1}{v_0} \int_{-\infty}^{\infty} \vec{F} dz = \frac{e}{c} \int_{-\infty}^{\infty} (B_x \hat{y} - B_y \hat{x}) dz = \Delta P_y \hat{y} + \Delta P_x \hat{x} \tag{8}$$

$$\Delta p_y = -\frac{2e}{c}\int_0^\infty(\partial\Phi^1/\partial x)dz$$
$$= -\frac{2e}{c}\int_0^\infty dz\int_{-\infty}^\infty d\,k_x\int_{-\infty}^\infty d\,k_y[i\,k_x A(k_x,k_y)\exp(i(k_x x + k_y y))\exp(-kz)] \quad (9)$$

$$\Delta p_x = \frac{2e}{c}\int_0^\infty(\partial\Phi^1/\partial y)dz$$
$$= \frac{2e}{c}\int_0^\infty dz\int_{-\infty}^\infty d\,k_x\int_{-\infty}^\infty d\,k_y[i\,k_y A(k_x,k_y)\exp(i(k_X x + k_Y y))\exp(-kz)] \quad (10)$$

Combining above equations gives

$$\partial\Delta p_y/\partial x - \partial\Delta p_x/\partial y = \frac{2e}{c}\int_{-\infty}^\infty d\,k_x\int_{-\infty}^\infty d\,k_y[kA(k_x,k_y)\exp(i(k_x x + k_y y))]$$
$$= \frac{2e}{c}\left[-\partial\Phi^1/\partial z\right]_{Z=0} = eB_0/c = [\nabla\times\Delta\vec{p}]_Z \quad (11)$$

and

$$\partial\Delta p_y/\partial y + \partial\Delta p_x/\partial x$$
$$= \frac{2e}{c}\int_{-\infty}^\infty d\,k_X\int_{-\infty}^\infty d\,k_Y\left[(k_x k_y/k - k_x k_y/k)A(k_x,k_y)\exp(i(k_x x + k_y y))\right] = 0 \quad (12)$$

where the z coordinate has been integrated. The above two equations can be easily understood as

$$\nabla\times\Delta\vec{p} = (eB_0/c)\hat{z}$$
$$\nabla\cdot\Delta\vec{p} = 0 \quad (13)$$

These final results look like Maxwell's equations for a magnetic field with current density $eB_o/4\pi$ along the z direction through the hole. So we may calculate Δp by integrating *the current density* $eB_o/4\pi$ in the hole. Simple cases are for circular and square holes. The maximum deflections (the

worst cases) occur at the circumference for the circular case and at the midpoint of an edge for the square case. They are:

$$|\Delta p / p| = (eB_0 L / mv_0 c) / 3.628 \qquad \text{for a square hole case}$$

$$|\Delta p / p| = (eB_0 D / mv_0 c) / 4 \qquad \text{for a circular hole case}$$

(14)

where L and D are the size of the square and the diameter of the hole, respectively. Note that there is not much difference between the square and circular cases. This is due to the fact that the deflection depends on how many lines of force an electron has to cross to get through the hole. This is primarily decided by the size of the hole and not by the shape. The above expressions are also valid for more than one hole provided that the magnetic material has infinite permeability and is not saturated.

As stated earlier in this section, the deflection resulting from the termination of the magnetic field should be kept low to maintain high spatial and spectral resolution. Since the angular dispersion due to the microscope's magnifying process is about 0.01 radian, we need to keep $|\Delta p/p|$ in equation (14) below 0.01. Practical values-15 Gauss for B_0 and 50 eV electrons-give D of 0.64 mm. In the practical design of the mesh, the saturation field and the permeability of the magnetic material, the resolution of the imaging detector, the desired energy resolution of the analyzer and the transparency of the mesh must be considered together.

3. Theory of double 90 degree spherical analyzers

The idea behind this imaging BPA is that two 90° spherical sectors are combined so that the first sector focuses a parallel beam of electrons which carries the image information onto the exit plane[14]. Then the electrons with the desired energy are energy filtered by an aperture. The second sector then reforms the image at the detector(Fig. 3). The imaging along the non-

dispersive axis works the same way as that of a standard spherical analyzer for which there is focusing up to second order[15]. It can be easily shown that the next error term is $L\beta^2$, where L is the size of the image and β angular dispersion of the electrons. For a small angular dispersion, this term is negligible. The energy filtering is performed along the dispersive axis.

For the focusing along the dispersive axis, consider a 180° sector. It is well known that a 180° sector acts as a lens which focuses a point source at it's entrance to a point at the exit. Therefore, a 90° sector will convert a point source into a parallel beam, and conversely, a parallel beam entering the spherical sector is focused to a point at the exit plane[14]. The lens equations for the 90° analyzer to second order are:

$$Y_2 / R_0 = \beta_1 + \Delta E / E_0 - (Y_1 / R_0)^2 + O(3) \quad (15)$$

$$\beta_2 = -Y_1 / R_0 + \Delta E / E_0 + O(3) \quad (16)$$

Here R_0 the radius of the main path, Y_1 and Y_2 are the electron coordinates in the entrance and exit plane of the 90° sector with the origins at the main path, respectively. β_1 and β_2 are the angles of the electrons in both planes with respect to the main path. $\Delta E = E' - E_0$ is the energy deviation of the beam with energy E' with respect to the pass energy E_o(Fig. 4). Note that in equation (15) Y_2/R_0 is proportional to $\Delta E/E_0$ except for the terms β_1 and $(Y_1/R_0)^2$. Once these two terms are kept small, Y_2/R_0 is linearly dependent on $\Delta E/E_0$. This means that the plane between the two sectors becomes the energy plane and the energy resolution is set by the angular dispersion of the incoming electrons, β_1, and the image size, Y_1^{max}. Energy filtering can be performed by moving an aperture along this plane. For our case β_1 is always smaller than 0.01 rad. Since only the dispersion along the dispersive axis affects the resolution, the actual resolution is improved by a factor of $4/\pi = 1.27$ for spherically symmetric angular dispersion.

The determination of the size of the energy selecting aperture expressed by Y_2/R_0 depends on the energy resolution described above. A big aperture would allow more electrons with different energies to pass through it, hence the energy resolution would decrease. A small

aperture would improve the energy resolution by reducing the band width. But reducing the size of the aperture below a certain value would not improve the energy resolution above a certain limit which is set by the angular dispersion of the incoming electrons and the size of images as discussed above. So the size of the aperture should be a value such that it gives a band width approximately same as the energy resolution. For our case, 1% of the radius of the main path gives 1.2 mm for the proper aperture size.

For the second sector, equations (15) and (16) may be rewritten as

$$Y'_2/R_0 = \beta'_1 + \Delta E/E_0 - (Y'_1/R_0)^2 + O(3) \qquad (15')$$

$$\beta'_2 = -Y'_1/R_0 + \Delta E/E_0 + O(3) \qquad (16')$$

where Y'_1, β_1', Y'_2, β_2' are new co-ordinates for the second sector(Fig. 4). Since $\beta'_1 = -\beta_2$ and $Y'_1 = -Y_2$, combining equations (15), (16), (15') and (16') gives

$$\begin{aligned} Y'_2/R_0 &= -\beta_2 + \Delta E/E_0 - (Y_2/R_0)^2 \\ &= Y_1/R_0 - (Y_2/R_0)^2 \\ &= Y_1/R_0 - \beta_1^{\,2} - (\Delta E/E_0)^2 - 2\beta_1 \Delta E/E_0 + O(3) \end{aligned} \qquad (17)$$

This equation shows that the position of an electron at the exit plane of the second sector, Y'_2/R_0, is equal to that at the entrance plane of the first sector, Y_1/R_0, except for the factor $(Y_2/R_0)^2$. This can be neglected since from equation (17) all the terms are of second order or smaller. Therefore, equation (17) shows the recovery of the image at the exit plane of the second sector. The key point of this analyzer is that the first order terms in the angular and energy deviations are canceled out by combining two spheres in opposite direction, so that the final position of an electron does not depend on the initial angle, β_1, and the energy deviation, $\Delta E/E$, in first order. This fact can be easily seen if the 90° sectors were combined in the same direction, that is, $\beta'_1 = \beta_2$ and $Y'_1 = Y_2$ rather than $\beta'_1 = -\beta_2$ and $Y'_1 = -Y_2$. Then we get:

$$Y'_2/R_0 = -Y_1/R_0 + 2\Delta E/E_0 - \beta_1^2 - (\Delta E/E_0)^2 - 2\beta_1\Delta E/E_0 + O(3) \qquad (18)$$

Notice that there is an additional first order term from the energy dispersion. So the image can not be reformed by a 180° sector unless the electrons are mono-energetic.

For practical operation of the analyzer, we do not move the physical apertures between two spheres in order to change the desired electron energy but change the pass energy while fixing the physical aperture on the main path. Fixing the physical aperture on the main path forces Y_2 to be the size of the aperture. This improves the spatial resolution since Y_2 serves as the error term on the second line of equation (17). By changing the potentials on the spheres(or the pass energy) while keeping the aperture on the main path, the desired electron energy can be selected while maximizing the spatial resolution. With the size of the physical aperture of $0.01R_0$, the spatial resolution is about 0.01% of the main path radius.

4. Fringe field effects.

For the non-imaging analyzers fringe field effects are not serious since the entrance apertures are small enough not to disturb the energy resolution, which is not the case for this imaging BPA. In the ideal case(where there is no fringe field), mono-energetic, parallel electrons are focused to a point by the first 90° sector. But in the real situation, as the electrons enter the analyzer, those entering closer to either the inner or outer sphere experience larger fringe fields than the electrons closer to the main path(a and c in Fig. 5). We performed a ray trace and the results show that these fringe fields cause the electrons to arrive at the energy plane(exit plane of the first sector) at reduced radii. Therefore, these electrons act as if they have lower kinetic energies than the electrons traveling along the main path. This fringe field effect can be interpreted as if electrons are entering an analyzer with no fringe field with certain initial angles to the

direction perpendicular to the entrance plane so that they arrive at the energy plane at reduced radii. The more that the electrons are affected by the fringe field, the larger are these initial angles. Furthermore, these initial angles are all negative in the coordinate system in Fig. 4. This fringe field effect does not affect the spatial resolution provided the energy aperture is kept on the main path as shown on the second line of equation (17) while it does affect the energy resolution as equation (15) includes the variable β_1.

Since this effect simply results in an energy dispersion in the image at the exit plane of the second sector, it is possible to make a map of this energy dispersion and use this map to correct the fringe field effect. This calibration map is a map of percentage errors in measured electron energies from the real values as a function of positions in the image and can be obtained by taking a series of images of a uniform mono-energetic input at different pass energies. This technique also automatically removes the size effect of images in the energy resolution which was discussed in section 3 so that the energy resolution is limited only by the angular dispersion of the electrons.

5. Test results using an electron gun

To test the analyzer, we used the test setup as shown in Fig. 6. The double 90° sectors with inner and outer radii of 88.27 mm and 145.4 mm, respectively(which gives mean radius of 116.8 mm), were constructed by Surface/Interface, Mountain View, CA. An electron gun with an Iridium coated filament from Apex Electronics was used as the electron source, which has a 0.7 eV energy width. The two dimensional detector is a resistive anode combined with double stage micro-channel plates. The distance from the electron gun to the entrance of the analyzer was about 0.90 m. To shield the earth's magnetic field, double steel tubes were used for the 0.90 m long electron path, and the analyzer has its own shielding. The operating electron energy was 500 eV and the potential at the main path was held at ground so that the pass energy was also 500 eV. With no magnetic field inside the tubes, the maximum electron angle should be less than 0.015

radian. Imperfect field shielding might have introduced additional small deviations.

First, the energy resolution was tested. An 1 mm slit was used for the energy aperture. 1 mm is about 0.86% of the main pass radius which is 116.8 mm. While holding the aperture on the main path and changing the pass energy, we recorded the total number of electrons at the detector. From Fig. 7 it is clear that the peak is not a symmetric Gaussian. Most of the dashed area comes from the fringe field effect. As discussed in section 4, the fringe field effect results in the electron distribution on the lower side of the main peak. Removing the emission in the dashed area gives a FWHM of 4.5 eV. For an image size of 12x12 mm^2(unaffected area by the fringe field effect) the angular dispersion is 0.01 rad and this gives an energy resolution of 1% of the pass energy. So FWHM of 4.5 eV is consistent with the calculated value of 5 eV.

Second, the spatial resolution was tested using a square grid pattern at the entrance of the analyzer. The grid pattern is a 10 line/inch nickel mesh. Fig. 8.a shows a 25x25 mm^2 image. This image was taken with a 35 mm diameter circular aperture rather than with the 1 mm slit aperture. This does not show the fringe field effect because the large aperture does not perform any energy selection. Fig. 8.b shows an image of the same grid pattern with the 1 mm slit aperture. The 1 mm aperture gives a smaller image since the aperture accepts only *500 eV electrons* and cuts out the fringe field affected electrons which act as if they are lower energy electrons as stated in section 4. The electrons eliminated from this area make up the tail of the curve in Fig. 7. When a spectrum is taken from an area which is not fringe field affected, we get the same spectrum as the one in Fig. 7 without the tail. So 1% energy resolution and 0.01% spatial resolution is achieved simultaneously only on the image size of about 12x12 mm^2 as can be seen in Fig. 8.b. If bigger images are necessary, one would need to use the methods described in section 4. No difference in image sharpness between these two images is noticed. Since, according to equation (17), the spatial resolution with a smaller aperture should be better than that with a larger one, one can guess that the spatial resolution is limited by that of the detector. The counting ratio between blocked and unblocked areas by the mesh is more than 1 to 10 and these counts in the blocked area are presumed due to the spatial resolution of the detector.

What little aberration is present in this image comes from non-linearity of the detector and the residual magnetic field in the analyzer chamber. This residual magnetic field poses another problem for the future. Since the analyzer eventually sits in a relatively high field(~15 Gauss) and it needs to be operated at a lower pass energy for a better energy resolution, the residual field effect will be bigger. So a good method of complete degaussing of the system would be essential for both energy and spatial resolution.

Acknowledgment

This work was partially supported under Air Force Contract No. AF 49620-86K-0019 and was performed at the Stanford Synchrotron Radiation Laboratory, which is supported by the Department of Energy, Office of Basic Energy Science, Division of Chemical Sciences. C.K. and P.P. acknowledge the support of that Office's Division of Material Science for this research. P.K. would like to acknowledge support from the Stanford University Center for Materials Research under NSF-MRL grant DMR-87-217359. C.K. would like to appreciate the help of R. Morris and M. Ackeret.

References

[1]M. Cardona and L. Ley, in **Photoemission in Solids I: General Principles,** M. Cardona, L. Ley, Eds.(Springer-Verlag, Berlin, 1978), pp. 1.

[2]R. L. Chaney, *Surf. Interface Anal.* **10**, 36(1977).

[3]H. Ade, J. Kirz, S. Hulbert, E. Johnson, E. Anderson and D. Kern, *Nucl. Instr. and Meth.* **A291**, 126(1990).

[4]R. Nyholm, M. Eriksson, K. Hansen, O.-P. Sairanen, S. Werin and A. Flodstrom, *Rev. Sci. Instrum.* **60**, 2168(1989).

[5]C. Capasso, G. Margaritondo, W. Ng and J. Underwood, *J. Vac. Sci. Technol.* **B9**, 1248(1991).

[6]I.W. Drummond, L.P. Ogden, F.J. Street and D.J. Surman, *J. Vac. Sci. Technol.* **A9**(3), 1434(1991).

[7]U. Gelius, B. Wannberg, P. Baltzer, H. Fellner-Feldegg, G. Carlsson, C.-G. Johnasson, J. Larsson, P. Munger and G. Vegerfors, *J. Electron Spectro. Relat. Phenom.* **52**, 747(1990).

[8]P. Coxon, J. Krizek, M. Humperson and I. R. M. Wardell, *J. Electron Spectro. Relat. Phenom.* **52**, 821(1990).

[9]P. Pianetta, I. Lindau, P.L. King, M. Keenlyside, G. Knapp and R. Browning, *Rev. Sci. Instrum.* 60, 1686(1989).

[10]G. Beamson, H. Q. Porter and D. W. Turner, *Nature* **290**, 556(1981).

[11]P. Kruit, and F.H. Read, *J. Phys. E: Sci. Instrum.*, **16**, 313(1983).

[12]P.L. King, **Photoelectron Microscopy**(Ph.D. Thesis, Stanford University, 1992).

[13]J.D. Jackson, **Classical Electrodynamics**, See Chapter 3. There is a similar problem in the chapter.

[14]E. Kisker, M. Campagna, W. Gudat, and E. Kuhlmann, *Rev. Sci. Instrum.*, **50**(12), 1979.

[15]B. Tonner, *Nucl. Instr. and Meth.* **A291**, 60(1990).

Fig. 1. The schematic of the MicroESCA^{TM} magnetic projection photoelectron microscope.

Fig. 2. A sheet of magnetic material separates two regions with asymptotic magnetic fields of zero on one side and B_o on the other side.

Fig. 3. The schematic of the double 90 degree spherical analyzer. Imaging electrons are entering from 15 Gauss region to a field free region through a magnetic mesh.

Fig. 4. Coordinates used in the calculation. Y'_1, β_1', Y'_2, β_2' are new co-ordinates for the second sector. Note that $Y_2 = -Y'_1$ and $\beta_2 = -\beta'_1$.

Fig. 5. Fringe field effects on mono-energetic imaging electrons. Electrons closer to the spheres(a and c) have shorter radii compared to the electrons closer to the main path(b).

Fig. 6. The testing setup of the analyzer.

Fig. 7. Counts as a function of pass energy. The tail(dashed area) on the lower energy side of the graph comes from the fringe field effect.

Fig. 8. (a) A 25x25 mm^2 image of a grid pattern at the entrance of the analyzer with a 35 mm energy aperture. The pattern was a 10 line/inch nickel mesh. This image contains 160x160 pixels. (b) same as (a) with 1 mm slit aperture. Dispersive axis is about 30 degree off to the right of the vertical direction. Some part of the image does not have counts. Electrons in this area are fringe field affected and, consequently, are eliminated by the energy aperture.

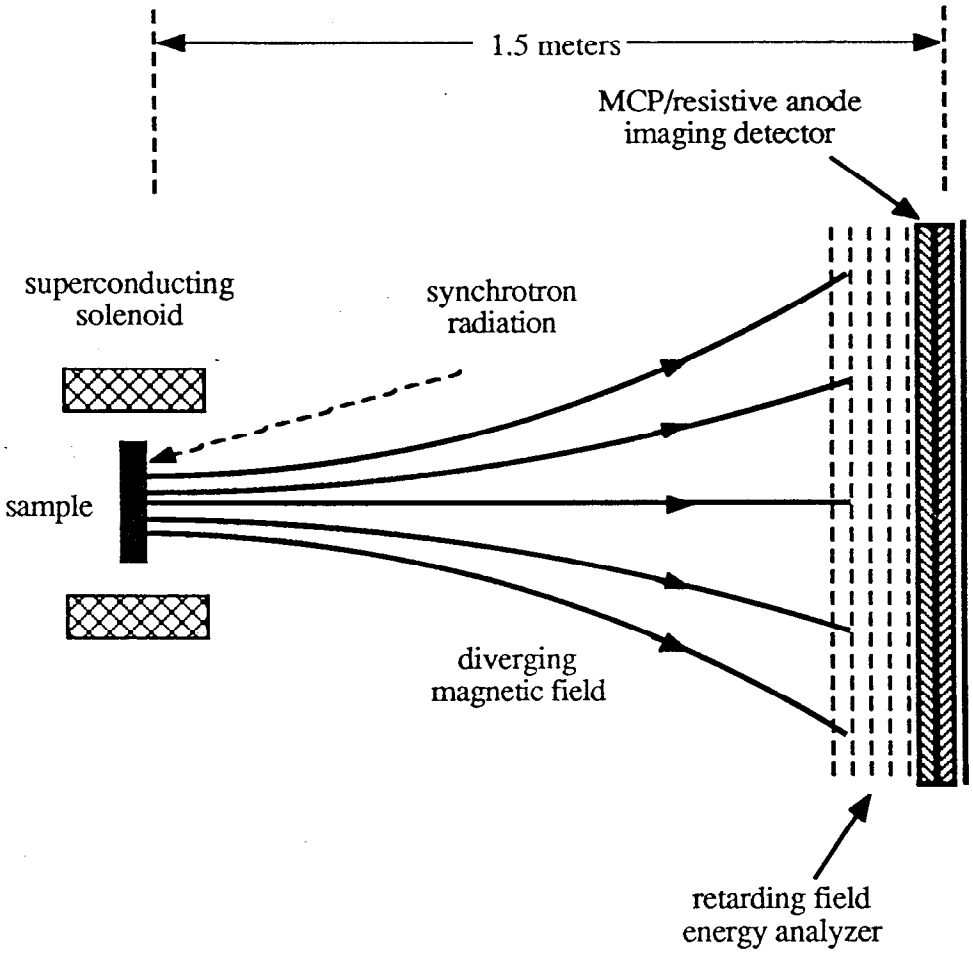
1.5 meters
MCP/resistive anode
imaging detector
superconducting
solenoid
synchrotron
radiation
sample
diverging
magnetic field
retarding field
energy analyzer

Fig. 1

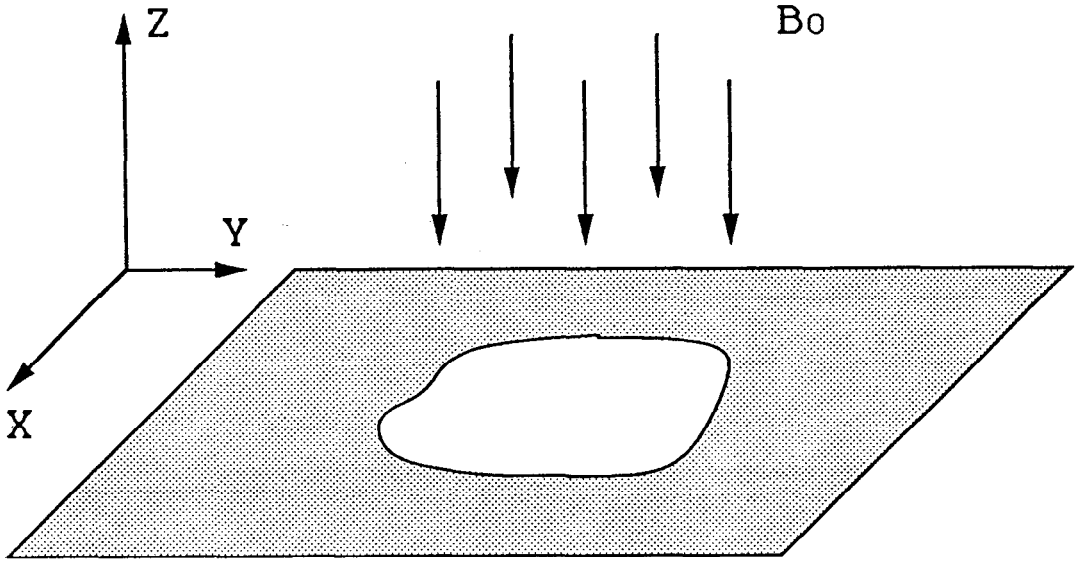

B = 0

Fig. 2

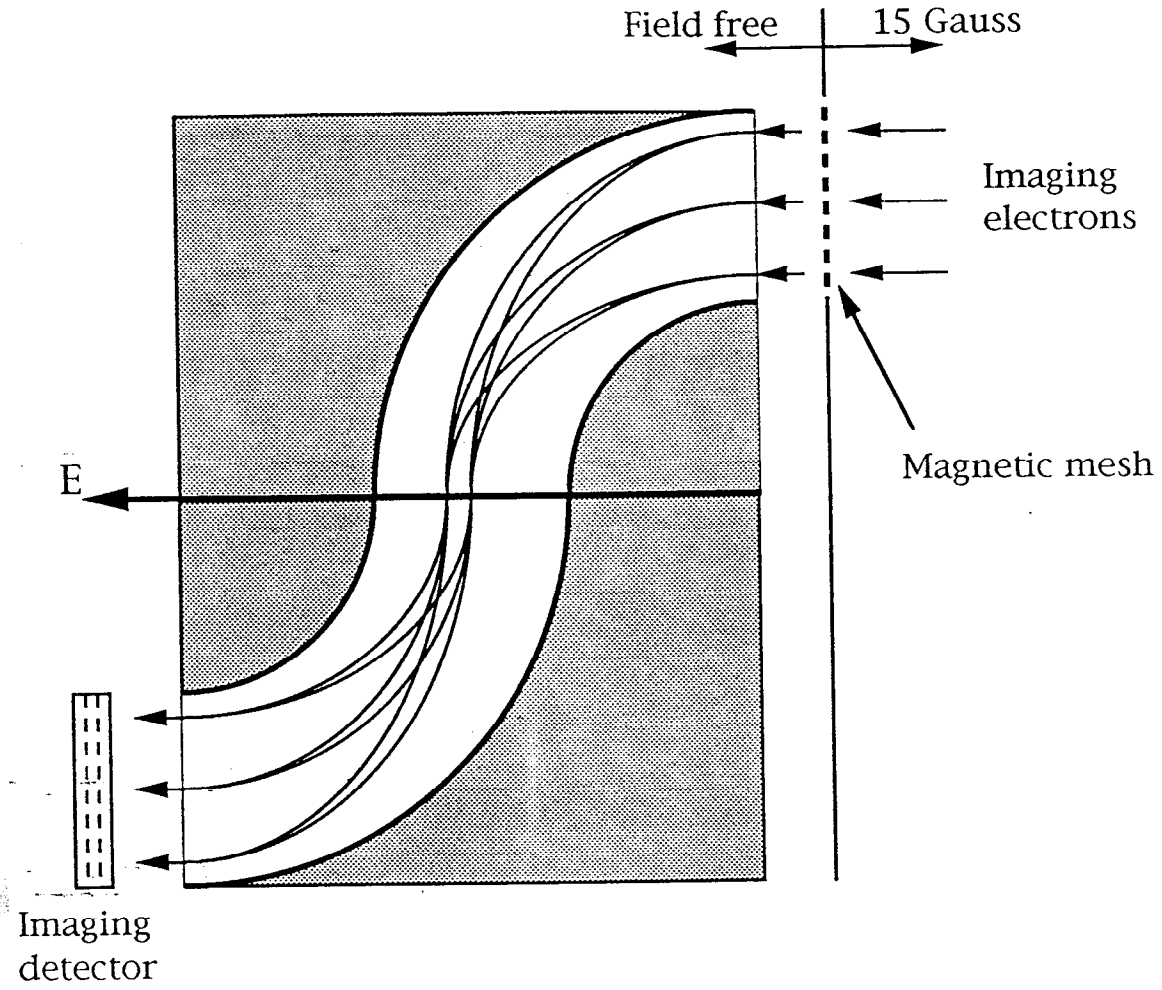
Field free
15 Gauss
Imaging
electrons
Magnetic mesh
E
Imaging
detector

Fig. 3

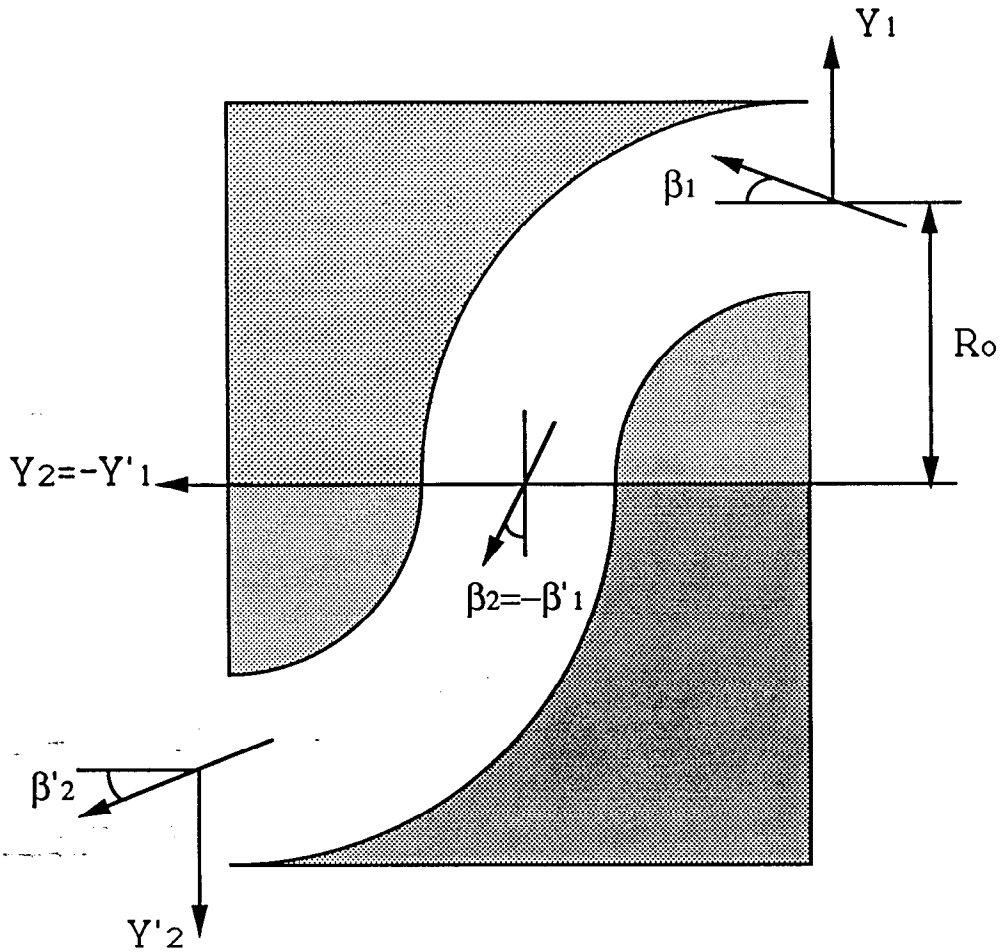

Fig. 4

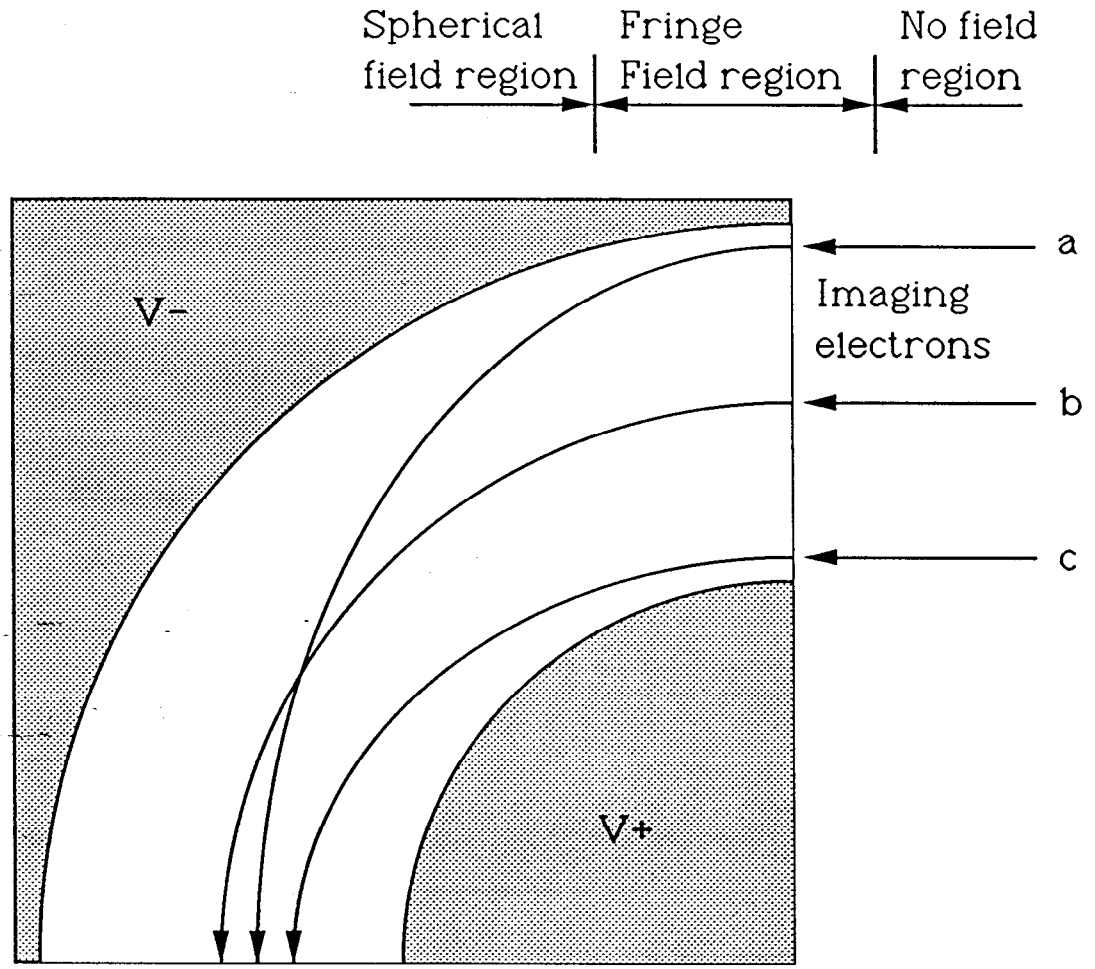
Spherical
field region
Fringe
Field region
No field
region
V-
V+
a
Imaging
electrons
b
c

Fig. 5

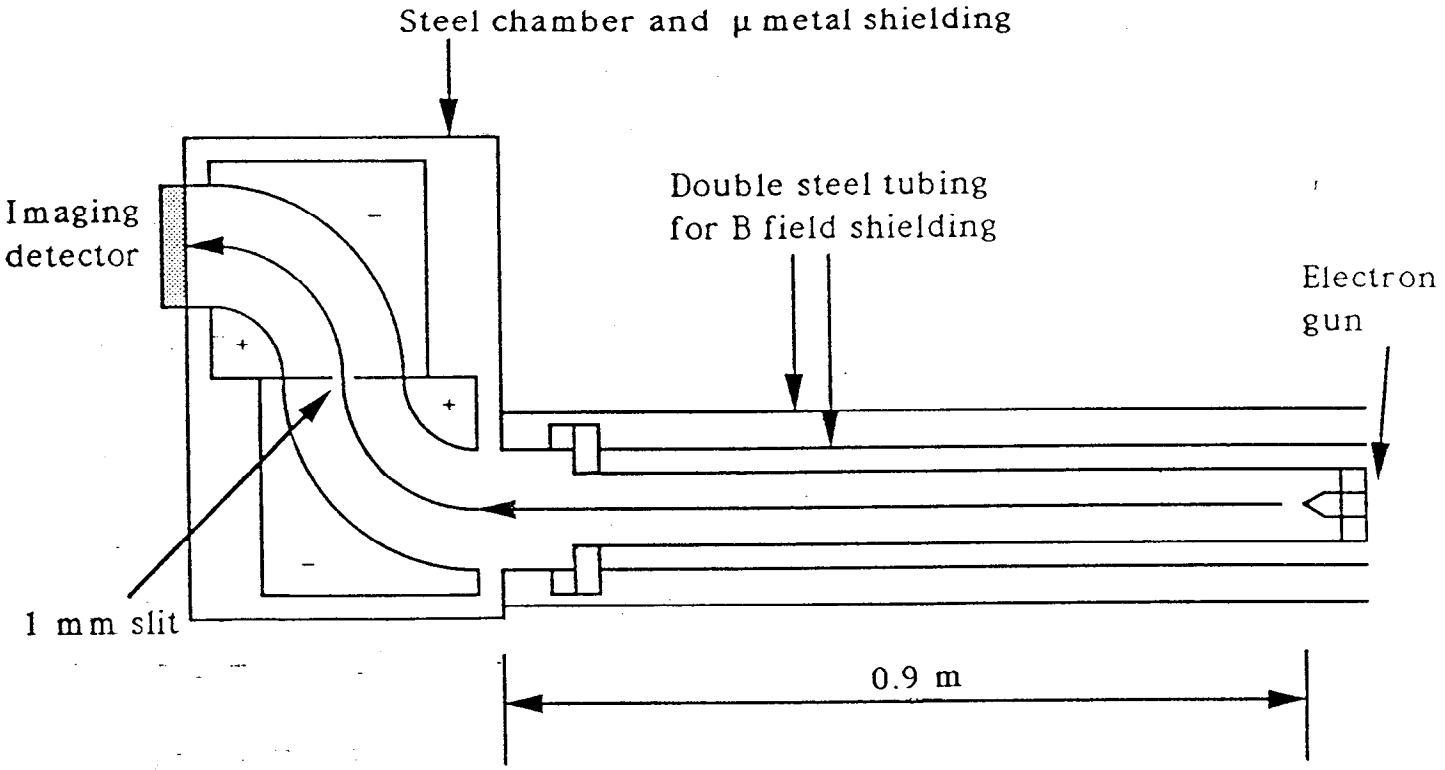
Steel chamber and μ metal shielding
Imaging detector
Double steel tubing for B field shielding
Electron gun
1 mm slit
0.9 m

Fig. 6

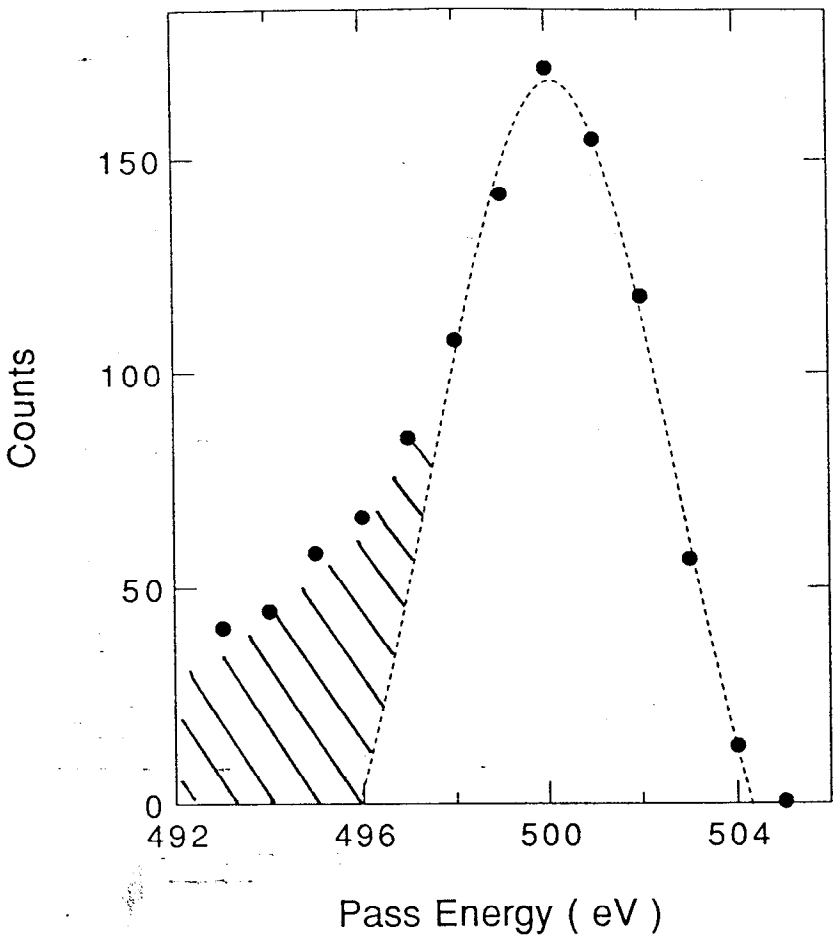

Fig. 7

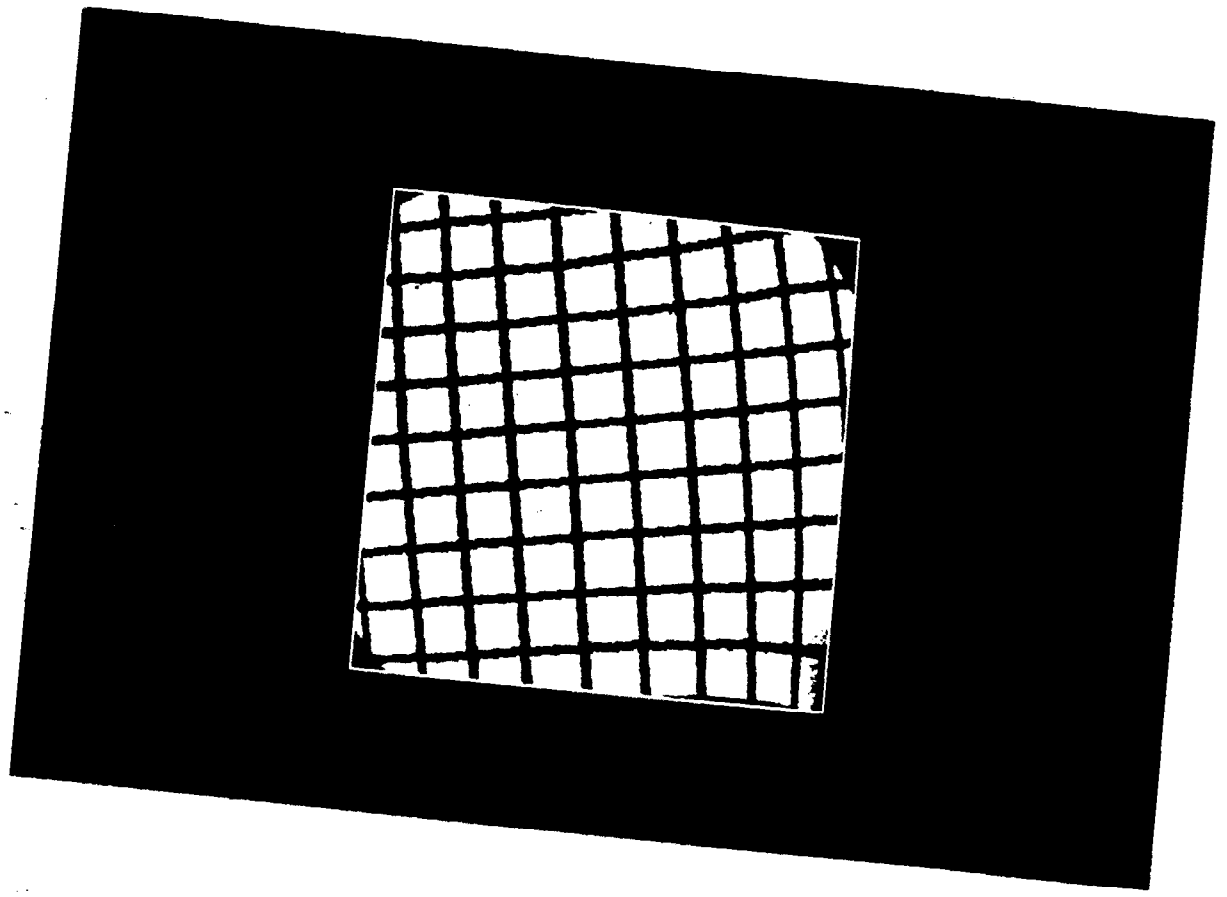

Fig. 8a

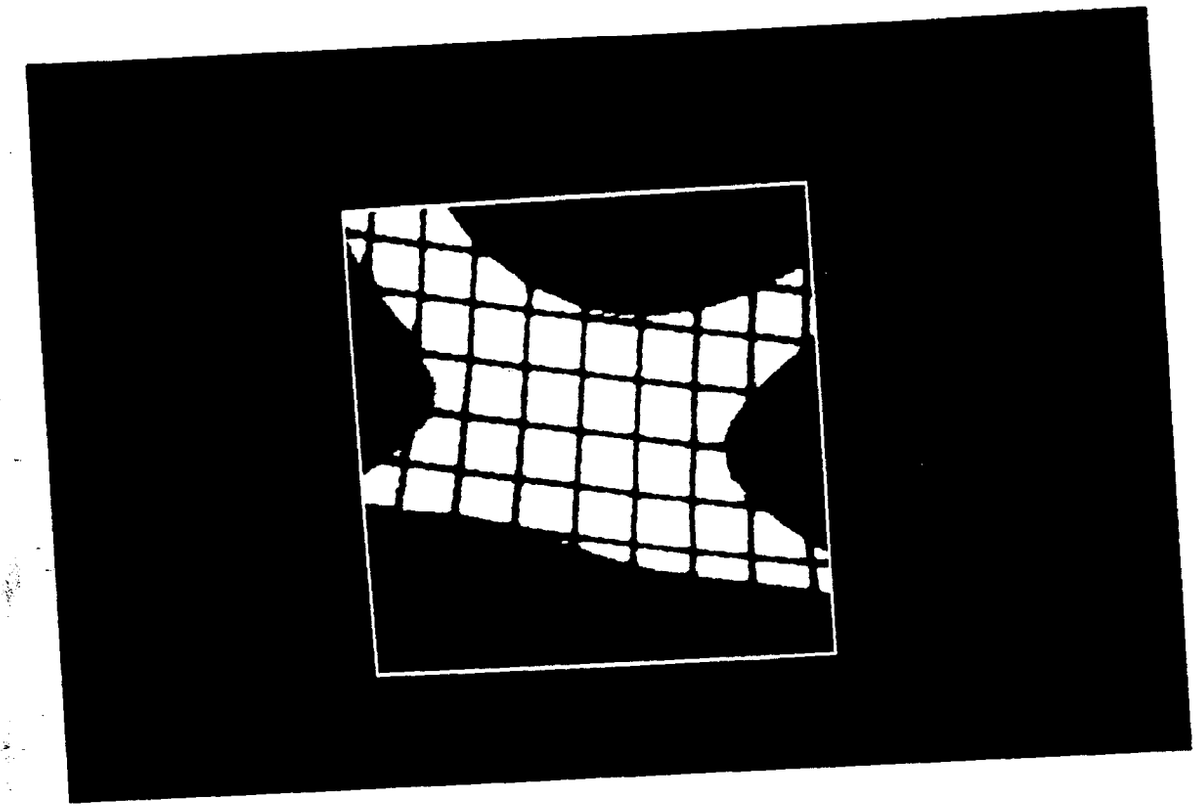

Fig. 8b